ROYAL SOCIETY
OF CHEMISTRY

PAPER

Check for updates

Z-scheme LaCoO$_3$/C$_3$N$_5$ for efficient full-spectrum light-simulated solar photocatalytic hydrogen generation

Rui Wang, [ac] Kexin Zhang, [a] Xin Zhong [b] and Fubin Jiang [*ab]

The development of photocatalysts with high activity and low cost is still a major challenge. Since its synthesis in 2019, C$_3$N$_5$ has become an emerging photocatalytic material and has been widely studied. In this work, we report on the preparation of LaCoO$_3$/C$_3$N$_5$ nanosheets and the use of LaCoO$_3$ instead of precious metals to improve photocatalytic hydrogen production activity. First, LaCoO$_3$ was successfully prepared by the sol–gel method and then a series of high-efficiency Z-type LaCoO$_3$/C$_3$N$_5$ heterojunction photocatalysts were synthesized by the solvothermal method. Various characterization techniques (XRD, FT-IR, SEM, TEM, EDS, XPS, UV-Vis DRS, BET, ESR) confirmed the formation between LaCoO$_3$ nanoparticles and C$_3$N$_5$ nanosheet heterostructures and interface interactions. In the photocatalytic water split test, 50 wt% LaCoO$_3$/C$_3$N$_5$ showed the highest photocatalytic activity of 956.11 μmol h^{-1} g^{-1}, which was 3.21 and 1.59 times that of LaCoO$_3$ and C$_3$N$_5$, respectively. This work not only designs an inexpensive and efficient LaCoO$_3$/C$_3$N$_5$ photocatalytic system for water splitting or other photocatalytic applications, but also provides ideas for constructing new material photocatalytic systems.

1. Introduction

With the rapid development of industry and the increasing industrialization of the economy and society, human demand for energy is increasing. Photocatalysis is an effective method for converting solar energy into chemical energy. To date, the most extensive research has involved solar photovoltaic cells and photocatalytic hydrolysis to produce hydrogen and carbon dioxide. Among them, photocatalytic water hydrogen production is an effective green and sustainable method with the potential to solve our current energy dilemma.[1–3]

Graphite carbon nitride is a typical metal-free organic polymer semiconductor photocatalyst.[4–7] The reason why it is widely used is that it has the advantages of a suitable band gap, high chemical stability during the visible light response and easy preparation.[8–11] Karthik Shankar's research group[12] changed the synthesis method to synthesize a new type of carbon nitride material, C$_3$N$_5$ is used for methylene blue degradation experiments. Compared with the previous C$_3$N$_4$, C$_3$N$_5$ has many advantages, when used as the electron transport layer (ETL) of halide perovskite solar cells, the performance of C$_3$N$_5$ is better than that of g-C$_3$N$_4$, especially for generating open-circuit light

voltages up to 1.3 V. The narrow band gap and two-dimensional structure of C$_3$N$_5$ make it an interesting air and high-temperature resistant semiconductor in optoelectronic applications, while its electronic-rich properties and on-chip cavity make it attractive for environmental applications. Siyun Qi *et al.*[13] demonstrated from first-principles calculations that C$_3$N$_5$ multilayers can serve as promising candidates to product hydrogen *via* photocatalytic water splitting reaction. Dazhong Sun *et al.*[14] demonstrated the most potential for overall water splitting to be the easiest to synthesize experimentally *via* formation energy calculation of 18 structures. At present, the research on C$_3$N$_5$ photocatalytic water splitting is still in the stage of computational chemistry. In this article, our systematic experiments verify the photocatalytic action and mechanism of C$_3$N$_5$ and its complexes.

Recently perovskite-type semiconductor materials have aroused great interest among researchers.[15–22] Because of their adjustable band gap, strong photocorrosion resistance and sufficient oxygen vacancies, they have become very promising photocatalysts.[23–28] With these characteristics, they are excellent materials for solar cells and photocatalytic reactions, and they have attracted great attention from researchers.

According to previous experimental reports, we believe that C$_3$N$_5$ is a potential photocatalytic hydrogen production catalyst. We used it to degrade water under full-spectrum light irradiation. A series of photocatalysts were prepared by combining perovskite and C$_3$N$_5$. First, C$_3$N$_5$ was prepared by the method reported by the Karthik Shankar group, and the perovskite photocatalytic material LaCoO$_3$ was prepared by the sol–gel

College of Chemistry, Beijing Normal University, Beijing, 100875, China. E-mail: jfb@bnu.edu.cn; Tel: +86 01058802850

Department of Chemistry, Faculty of Arts and Sciences, Beijing Normal University, Zhuhai, 519087, China

Institute of Chemical Engineering and Technology, Xi'an Jiao Tong University, Xi'an, 710049, China

method. Then, the perovskite was loaded on C_3N_5 by ultrasonic dispersion, overnight stirring, and the solvothermal method. $LaCoO_3/C_3N_5$ photocatalysts with different mass percentages of 10 wt%, 30 wt%, 50 wt%, 70 wt%, and 90 wt% were added. After that, the photocatalytic performance of C_3N_5 under full-spectrum light irradiation and the optimal doping ratio of the catalyst after doping were tested by photocatalysis. In addition, we carried out XRD, SEM, TEM, EDS, XPS, PL, FT-IR, UV-Vis DRS, EPR.

2. Experimental section

2.1. Materials

Lanthanum nitrate hexahydrate (purity > 99.99%), cobalt nitrate hexahydrate (purity > 99.99%), citric acid (purity > 99%), and urea (purity > 99%) were used. All other reagents used in this study were analytically pure and used without further purification. Deionized water was used for all of the experiments.

2.2. Catalyst preparation

2.2.1. Preparation of C_3N_5

(1) Synthesis of melem (2,5,8-triamino-s-heptazine). A certain amount of melamine was heated in a covered alumina crucible at 425 °C overnight. A light yellow powder was obtained, crushed and suspended in deionized water. The suspension was refluxed for several hours to remove unreacted melamine and other impurities. The resulting white product was collected by centrifugation and dried at room temperature.

(2) Synthesis of 2,5,8-trihydrazino-s-heptazine. Take 1.6 g (7.5 mmol) of the product melem from the previous step in 15 mL (0.25 mol) of 55% hydrazine hydrate aqueous solution, and seal it in a 25 mL Teflon lined autoclave. The autoclave was heated in an oven at 140 °C for 24 hours and then cooled, and the obtained light yellow solution suspension was transferred to a 100 mL beaker. Add 10% HCl to keep the pH between 1–2. The solution was filtered to remove unreacted solid residues containing residues. The filtrate was precipitated by adding 10% NaOH solution and maintaining the pH between 7.5–8.5. The resulting solid was dissolved in HCl again, filtered and reprecipitated in NaOH, repeated three times. Finally, the obtained solid was washed several times with deionized water and ethanol and dried under vacuum.

(3) Synthesis of C_3N_5 polymer. The C_3N_5 polymer was synthesized by heating 2,5,8-trihydrazino-s-heptazine (2,5,8-trihydrazino-sheptazine) at a temperature of 450 °C and a heating rate of 2 °C at 450 °C for 2 hours. The obtained orange powder can be used in subsequent experiments without further manipulation.

2.2.2. Preparation of $LaCoO_3$.
(1) Calculate the required mass of the reactants in strict accordance with a ratio of cobalt nitrate, lanthanum nitrate and citric acid at 1 : 1 : 2. The above three reactants were weighed and dissolved in 10 mL of secondary water to obtain a purple-red solution. During the preparation process, other ions should be preventing from mixing into the solution, and the instrument should be rinsed with water twice before use.

(2) Transfer the solution from the previous step to a round-bottom flask, heat it in a water bath at 80 °C, and stir it magnetically until the solution becomes a purple sol.

(3) Pour the sol obtained in the previous step into a clean ceramic crucible and dry it at 120 °C in a blast drying box to obtain a swollen purple dry gel, which is ground for later use.

(4) The obtained solid was calcined in a muffle furnace at 400 °C for 4 hours and then at 700 °C for 4 hours. After the machine was naturally cooled, black $LaCoO_3$ powder was collected.

2.2.3. Preparation of the $LaCoO_3/g-C_3N_4$ composites.
$LaCoO_3/C_3N_5$ with different weight ratios was prepared by the solvothermal method. Certain amounts of $LaCoO_3$ and C_3N_5 were separately dispersed in 10 mL of absolute ethanol and sonicated for 30 minutes. Then, the $LaCoO_3$ suspension was slowly added to the C_3N_5 ethanol solution under stirring, and the mixed solution was sonicated again for 30 minutes. Subsequently, the mixed solution was stirred at ambient temperature for 12 hours, transferred to a hydrothermal kettle and heated at 120 °C for 6 hours. Finally, the resulting mixture was centrifuged and dried at 80 °C for 12 hours. $LaCoO_3/C_3N_5$ nanosheet samples with different $LaCoO_3$ contents of 10, 30, 50, 70 and 90 wt% were prepared according to the above method.

2.3. Characterization

The crystal structures and phase composition of the obtained samples were determined by means of a Shimadzu Maxima X-ray diffractometer (XRD 7000) with Cu Kα radiation at a current of 30 mA and a voltage of 40 kV. The surface morphologies and microstructures of the samples were characterized by scanning electron microscopy (SEM, HITACHI S-4800) and transmission electron microscopy (TEM, FEI Talos F200S) in conjunction with energy dispersive spectroscopy (EDS). X-ray photoelectron spectroscopy (XPS) analysis was performed with a ThermoFisher electron spectrometer (XPS, ESCSLAB 250Xi) equipped with a monochromatized micro-focused Al Kα X-ray source, and the binding energy was referenced to the C 1s peak at 284.6 eV. Fourier transform infrared (FT-IR) spectroscopy was carried out by using an infrared spectrometer (Shimadzu IRAffinity-1). Using a UV-2600 spectrophotometer (Shimadzu, Japan) ($BaSO_4$ as the reflection standard), the optical properties of the prepared samples were tested by UV-Vis DRS. PL spectroscopy was performed at room temperature on an FS5 fluorescence spectrophotometer with a 500 W xenon lamp light source and an excitation wavelength of 300 nm. In a standard three-electrode system, a CHI660E electrochemical workstation was used with platinum mesh as the counter electrode, silver/silver chloride electrode as the reference electrode, and 5 mg each $LaCoO_3$, $g-C_3N_4$ and $LaCoO_3/g-C_3N_4$-20wt% were dissolved in 800 μL of distilled water, 200 μL of isopropanol and 30 μL of Nafion mixed solution. After ultrasonic treatment, it was dropped on the glassy carbon electrode as a working electrode. Use 0.1 mol L^{-1} Na_2SO_4 solution as the electrolyte. The width of the excitation and emission slit is 5 nm. The H_2 yield was detected on a Shimadzu gas chromatograph (GC-2014C) by manual injection. The

electron spin resonance spectrum was measured by an electron paramagnetic resonance spectrometer (Bruker E500).

2.4 Photocatalytic experiment

The photocatalytic activity of the as-prepared samples was evaluated by hydrogen production by light-driven water splitting. In this article, all water splitting experiments were performed at room temperature with magnetic stirring during light irradiation. The light source was a 300 W xenon lamp (PLS-SXE300) using full-spectrum ($250 < \lambda < 1200$ nm) simulated sunlight to perform the photocatalysis experiments. The specific operation parameters were as follows: First, 0.03 g of the prepared catalyst was placed in a custom-made quartz round-bottom flask and sonicated to suspend it in 30 mL of 10% CH_3OH aqueous solution in the dark, and nitrogen gas was passed through the solution for 30 min to remove the dissolved oxygen. A gas chromatograph equipped with a molecular sieve column and TCD detector was used to monitor the H_2 precipitation rate every hour. We used a manual injection method with a gas injector. It is worth mentioning that each material was subjected to three photocatalytic experiments to eliminate unexpected factors and enhance the reliability of the experimental data.

3. Results and discussion

3.1 Scanning electron microscopy (SEM) analysis

Fig. 1(a) and (b) show the structure of C_3N_5. The overall structure resembles a layered structure, with many layers converging into a large flat structure. In Fig. 1(c), the pure $LaCoO_3$ prepared by the sol–gel method is a collection of many nanoscale ellipsoids. Each ellipsoidal particle has a uniform particle size, and the particles grow tightly together to form a two-dimensional
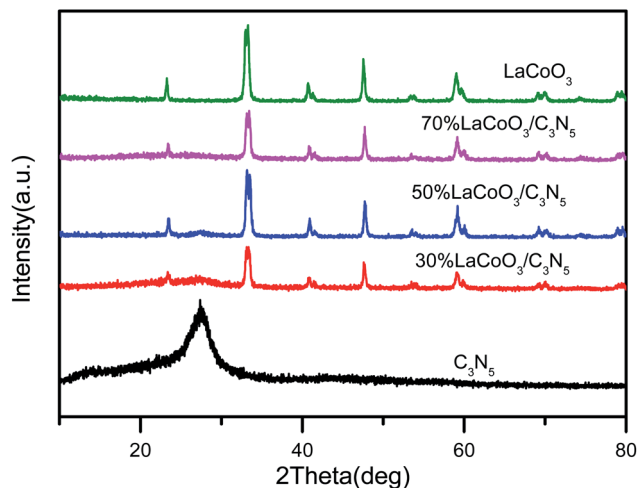

Fig. 2 XRD patterns of C_3N_5, $LaCoO_3$ and 30, 50, 70 wt% $LaCoO_3/C_3N_5$ powder.

nanolayered structure. From Fig. 1(d), we can observe that the $LaCoO_3$ nanoparticle layer is divided into small pieces, and these small pieces grow vertically on the C_3N_5 nanosheets. This structure can contribute to the photocatalyst's absorption of light, the effective separation of electron and hole pairs and the migration of electrons and holes.

3.2 X-ray diffraction (XRD) analysis

The crystal structures of pure $LaCoO_3$, C_3N_5 and $C_3N_5/LaCoO_3$ with different weight ratios were characterized by X-ray diffraction (XRD), as shown in Fig. 2. The X-ray powder diffraction characteristic curve of C_3N_5 shows a main peak at 27.4°, which can be attributed to the (0 0 2) crystal plane of
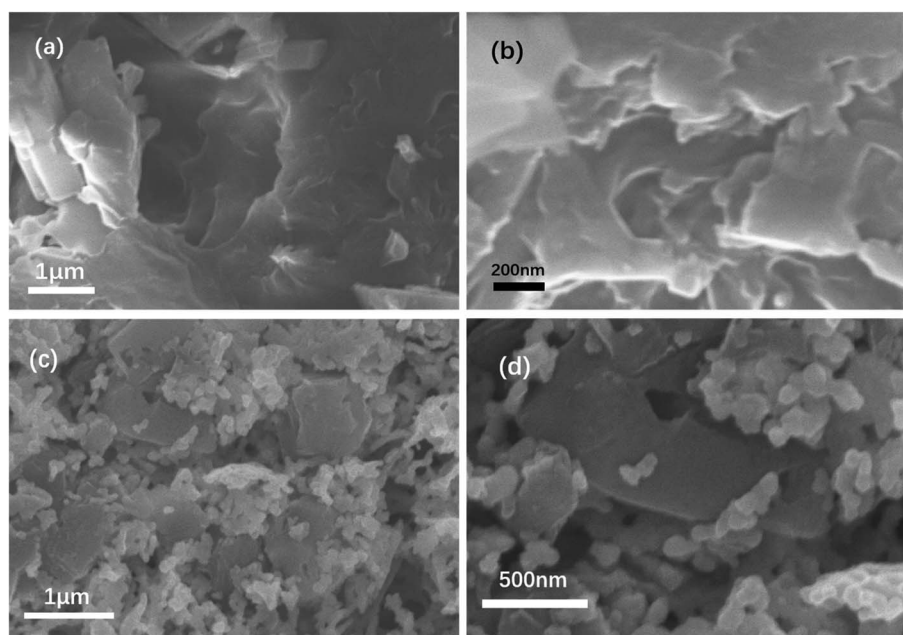

Fig. 1 (a and b) C_3N_5, (c) $LaCoO_3$, and (d) 50% $LaCoO_3/C_3N_5$ scanning electron microscopy images.

C_3N_5.[26] Each XRD diffraction peak of $LaCoO_3$ is highly consistent with the crystal phase of JCPDS no. 84-0848, and there are no other diffraction peaks, indicating that the prepared sample is pure $LaCoO_3$.[27–32] Interestingly, after the combination of $LaCoO_3$ and C_3N_5, the peak intensity of $LaCoO_3$ is slightly reduced, but the characteristic peak of C_3N_5 cannot be clearly observed in the compound 70 wt% $LaCoO_3$/C_3N_5, which may be due to its low crystallinity and lower amount of C_3N_5 doping.

3.3 Transmission electron microscope (TEM) analysis

We used TEM and HRTEM to further explore the characteristics of the catalyst morphology, element composition, composition structure, and particle size. In Fig. 3(a), $LaCoO_3$ shows an obvious ellipsoidal structure, and the particle size distribution range of the ellipsoid is 70–140 nm. In the HRTEM image of Fig. 3(b), we can observe that the spacing between adjacent lattice fringes is fixed, and the distance between adjacent lattice fringes can be obtained by measurement, that is, the plane
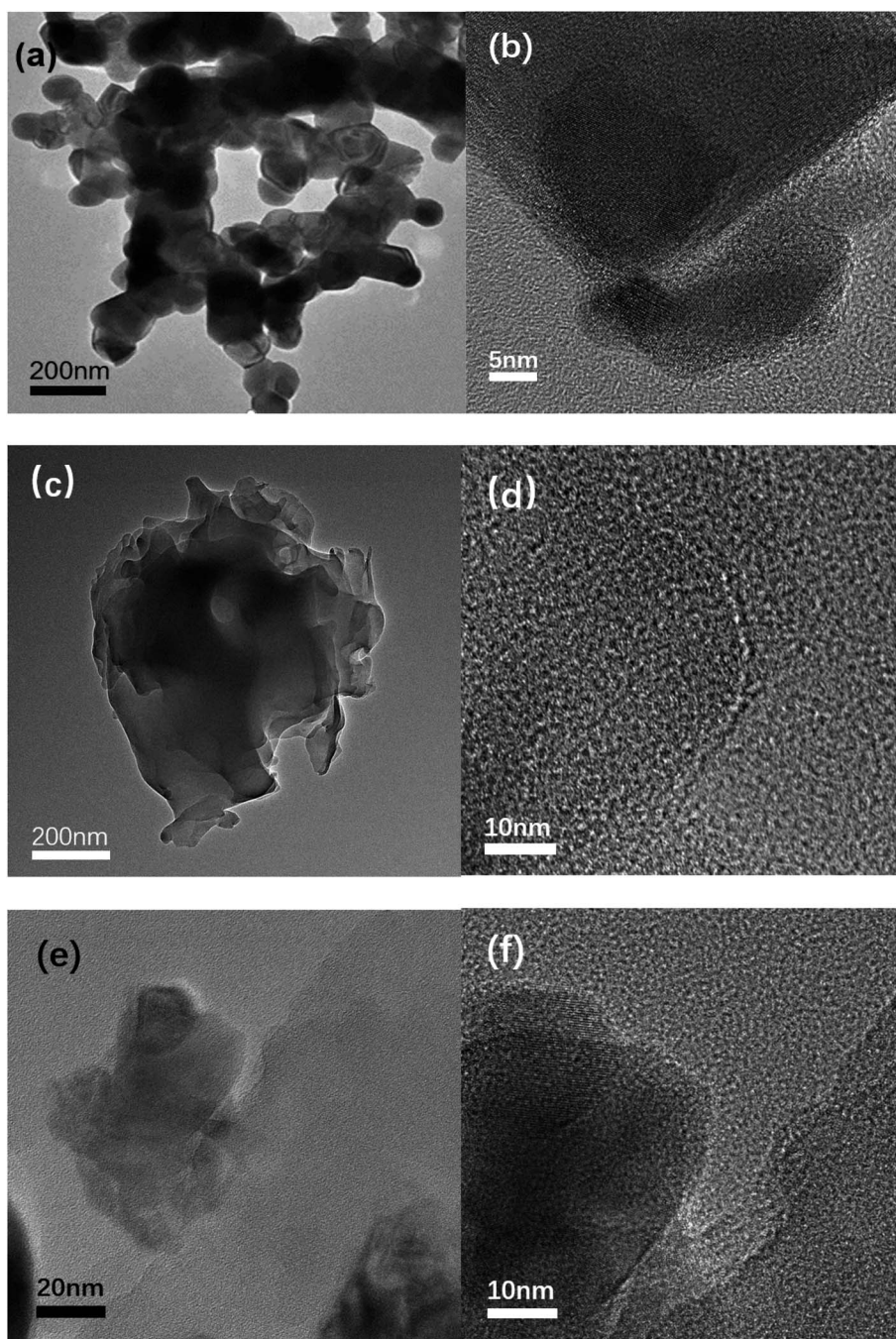

Fig. 3 (a) TEM image and (b) HRTEM image of $LaCoO_3$; (c) TEM image and (d) HRTEM image of C_3N_5; (e) TEM image of the $LaCoO_3$/C_3N_5-50wt% composite material, (f) HRTEM image.
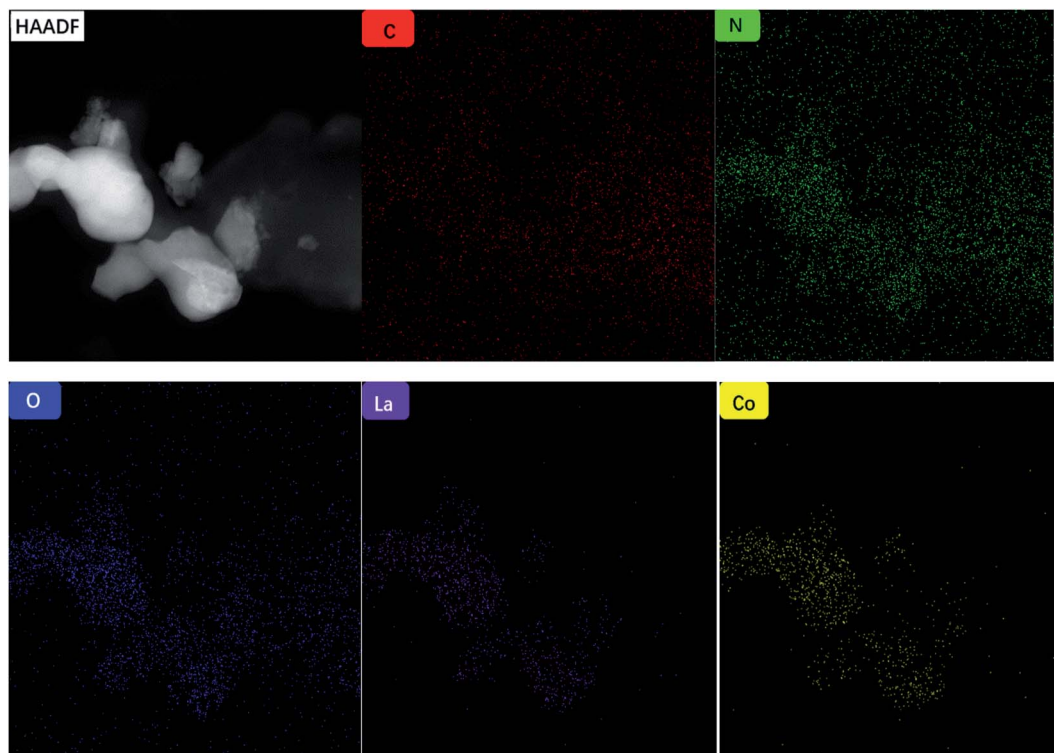
Fig. 4 50% $LaCoO_3/C_3N_5$ mapping image.

spacing is approximately 0.27 nm, consistent with the crystal plane (1 0 4). As shown in Fig. 3(c) and (d), the C_3N_5 transmission electron microscope shows a clear layered structure, resembling laver. In Fig. 3(e) and (f), crystal lattice plane separation can be observed at the interface between $LaCoO_3$ and C_3N_5. We can observe that the plane spacing between adjacent lattice fringes is approximately 0.27 nm, which is consistent with the crystal plane (1 0 4). Fig. 4 shows the element distribution image of 50% $LaCoO_3/C_3N_5$. The distribution of different elements can be seen from the figure.

3.4   X-ray photoelectron spectroscopy (XPS) analysis

To determine the chemical state of the elements, the surface chemical composition and the interaction between $LaCoO_3$ and C_3N_5, we performed XPS spectroscopic characterization, and the results are depicted in Fig. 5. All binding energies were corrected at 284.8 eV relative to the C 1s peak. The 50 wt% $LaCoO_3/C_3N_5$ composite material is comprised of La, Co, O, C and N. The high-resolution C1s spectrum of pure C_3N_5 can be divided into two main peaks at approximately 284.8 eV and 288.0 eV. The C 1s peak at 284.8 eV is attributed to the C–C bond in sp^3, and the peak at 288.0 eV is attributed to the sp^2-type C=N bond. The high-resolution N 1s spectrum of the C_3N_5 sample shown in Fig. 5(c) can be divided into three main peaks. We specified the N 1s peak with the lowest binding energy (398.6 eV) for the C–N bond and the central peak (399.3 eV) for the sp^2-type C=N bond.[33–35] The peak with the largest binding energy is at 401.0 eV, which comes from the amorphous CN network. The nitrogen is surrounded by three carbons.

However, a relatively strong sp^2 peak is formed due to the N=C–N type aromatic carbon, which constitutes C_3N_5, which is similar to the skeleton of carbon nitride. The HR-XPS spectrum of the core energy level in the N 1s region after peak splitting shows two peak components, located at 398.7 and 400.25 eV. The peak with a binding energy of 398.7 eV is attributed to the tertiary nitrogen N–(C)$_3$ and the secondary C=N–C nitrogen present in the aromatic ring structure, while the other peak at 400.2 eV is attributed to the presence of the main residues –NH$_2$ and bridging CN=N in NC. The two XPS peaks located at 531.6 and 532.4 eV in the O 1s region are related to the adventitious oxygen and –OH groups adsorbed on the surface.

The spectrum of the pure $LaCoO_3$ sample can be divided into three peaks: the one with the lowest binding energy (approximately 528.9 eV) is caused by lattice oxygen atoms on the surface, and the other (approximately 531.3 eV) is attributed to hydroxyl oxygen. The high-resolution O 1s spectrum of $LaCoO_3/C_3N_5$ shows two main features at 528.9 eV and 531.7 eV, which are attributed to lattice oxygen atoms and hydroxyl oxygen on the surface, respectively. It is worth mentioning that the hydroxyl–oxygen bond peak position in the 50 wt% $LaCoO_3/C_3N_5$ spectrum increased by 0.4 eV, which indicates that the chemical environment changed after being combined with $LaCoO_3$. The typical high-resolution XPS La 3d spectrum of a 50 wt% $LaCoO_3/C_3N_5$ sample shows two shoulder peaks. The vibration characteristics are located at 830–840 eV and 850–857 eV. The peaks can be divided into two distinct peaks at 833.7 eV and 837.3 eV and 850.4 eV and 854.2 eV, corresponding to the binding energies of La $3d_{5/2}$ and La $3d_{3/2}$, respectively,
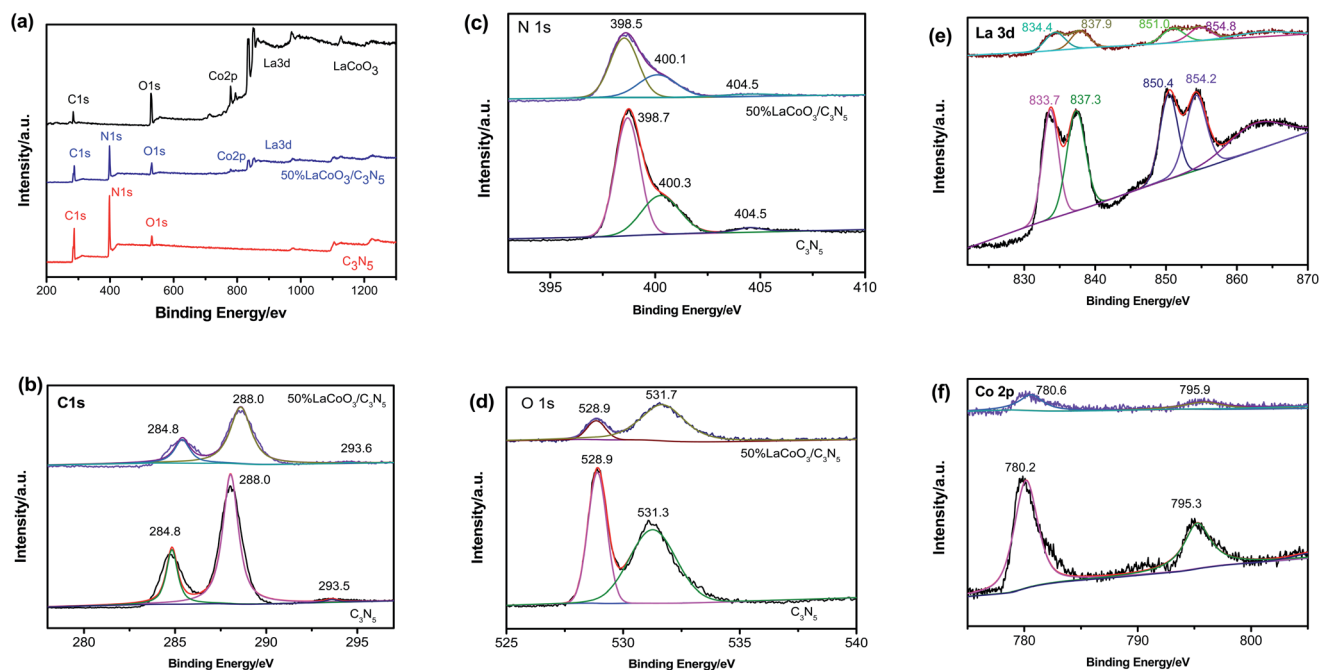
Fig. 5 (a) XPS full spectrum of LaCoO$_3$/C$_3$N$_5$-50wt% and pure LaCoO$_3$, C$_3$N$_5$; high-resolution spectra of (b) C 1s and (c) N 1s of LaCoO$_3$/C$_3$N$_5$-50wt% and pure C$_3$N$_5$; high-resolution XPS spectra of (d) O1s (e) La 3d and (f) Co 2p of LaCoO$_3$/C$_3$N$_5$-50wt% and pure LaCoO$_3$.

confirming the existence of La^{3+} in the crystal structure.[28–30] For the high-resolution Co 2p spectrum of the 50 wt% LaCoO$_3$/C$_3$N$_5$ sample. Fig. 5f, there are two main peaks at 780.2 eV and 795.3 eV, which are attributed to the typical shaking of the Co^{3+} structure at 787.2 eV.[30,31] In short, the XPS results further proved that the LaCoO$_3$/C$_3$N$_5$ composite material was successfully obtained.

3.5 Fourier infrared spectroscopy (FT-IR) analysis

The FT-IR results of pure LaCoO$_3$, C$_3$N$_5$ and LaCoO$_3$/C$_3$N$_5$ with different mass ratios are shown in Fig. 6. For pure C$_3$N$_5$, the characteristic peaks at 1257.64, 1332.22, 1419.67 and 1637.63 cm^{-1} consistently have aromatic CN tensile vibration modes. The peak at approximately 3151.82 cm^{-1} is attributed to the tensile and flexural vibrations of N–H, which are derived from uncondensed terminal amino groups. In addition, the respiratory vibration of C$_3$N$_5$ has a characteristic absorption peak at 808.21 cm^{-1}. The characteristic peak of LaCoO$_3$ at 594.10 cm^{-1} is related to the bending and tensile vibration of Co–O, which corresponds to the perovskite structure. As the content of C$_3$N$_5$ in the LaCoO$_3$ sample increases, the peak of the composite material gradually becomes sharper.[33,34]

3.6 UV-Vis diffuse reflectance spectrum (UV-Vis DRS) analysis

As shown in Fig. 7(a), the solid ultraviolet diffuse reflectance spectra of C$_3$N$_5$, LaCoO$_3$ and 50 wt% LaCoO$_3$/C$_3$N$_5$ composite materials were measured in the range of 250–600 nm by UV-Vis diffuse reflectance spectroscopy. It is worth noting that for pure LaCoO$_3$, almost all ranges of light can be absorbed, showing excellent photoelectric properties. The LaCoO$_3$/C$_3$N$_5$ composite

material has similar absorption characteristics to LaCoO$_3$. Compared with pure LaCoO$_3$, the absorption edge of the LaCoO$_3$/C$_3$N$_5$ composite shows a redshift, which indicates that the absorption of the LaCoO$_3$/C$_3$N$_5$ composite can absorb more visible light by moving.

The band-gap energy (E_g) of the semiconductor is determined according to the Kubelka–Munk equation, as shown below:
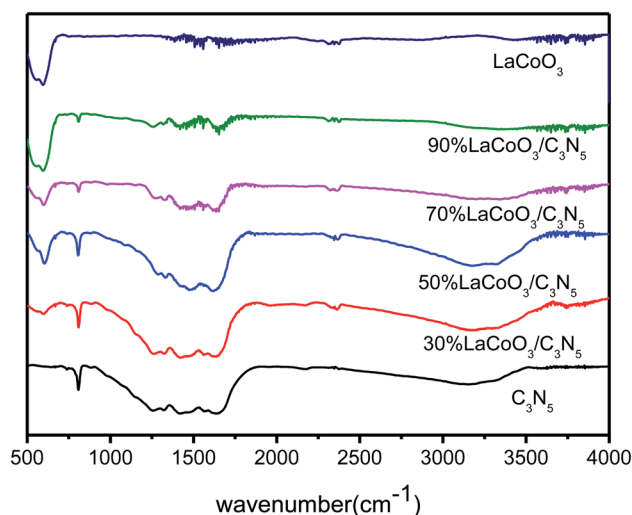
$$(\alpha h v)^{1/n} = A(h v - E_g) \tag{3.1}$$

Fig. 6 FT-IR spectra of C$_3$N$_5$, LaCoO$_3$ and 30, 50, 70, and 90 wt% LaCoO$_3$/C$_3$N$_5$.
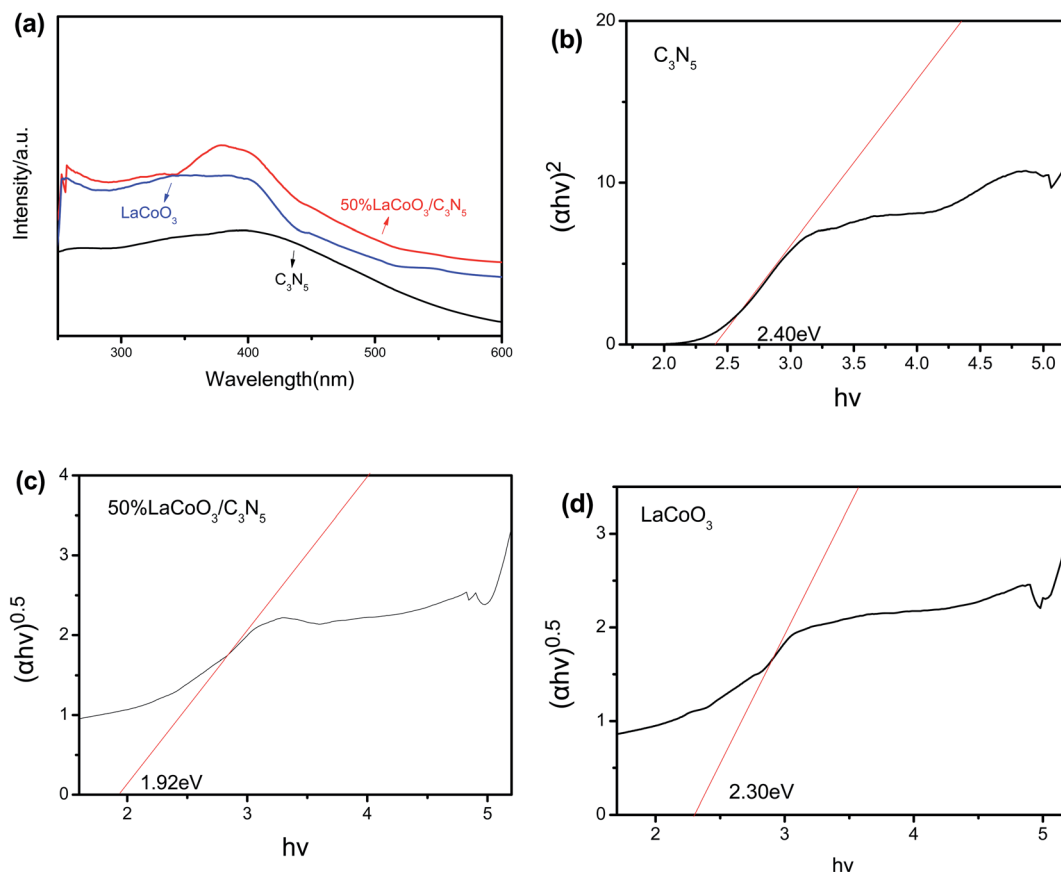
Fig. 7 (a) Solid ultraviolet diffuse reflection of $LaCoO_3$, C_3N_5 and $LaCoO_3/C_3N_5$ composites; (b) C_3N_5 (c) $LaCoO_3/C_3N_5$-50wt% (d) band gap energy (E_g) of $LaCoO_3$.

Here, α, h, υ, A, E_g, and n represent the absorption coefficient, Planck's constant, incident light frequency, constant, band-gap, and integer, respectively. The value of n mainly depends on the electronic transition structure of different semiconductors. If the band gap is a direct transition, then $n = 1/2$; if the band gap is an indirect transition, then $n = 2$. Fig. 7(b) shows the calculated detailed band-gap E_g values of C_3N_5, $LaCoO_3$ and $LaCoO_3/C_3N_5$-50wt%, which are approximately 2.40 eV, 2.80 eV and 1.82 eV, respectively. The E_g value obtained from the composite material is relatively small. In addition, the VB and CB potentials of the semiconductors can also be obtained from the following empirical formula:

$$E_{CB} = \chi - E^\theta - 0.5E_g \qquad (3.2)$$

$$E_{VB} = E_{CB} + E_g \qquad (3.3)$$

Among them, E_{CB} and E_{VB} represent the edge potentials of semiconductors CB and VB, respectively. χ is the

electronegativity of the semiconductor. According to ref. 35–37, the χ values of pure $LaCoO_3/C_3N_5$ can be obtained, which are approximately 4.59 eV and 5.64 eV, respectively. E^θ is the energy of a free electron with a hydrogen scale ($\sim$4.5 eV relative to NHE), and E_g is the band-gap energy of the semiconductor.

The values of χ, E_{CB}, and E_{VB} were calculated and are displayed in Table 1. The results show that the CB edge potential of C_3N_5 (-1.11 eV) is more negative than that of $LaCoO_3$ (-0.26 eV), while the potential edge of VB $LaCoO_3$ (2.54 eV) is more positive than that of C_3N_5 (1.29 eV).

3.7 Brunauer–Emmett–Teller (BET) surface area and Barrett–Joyner–Halenda (BJH) pore size distribution analysis

The parameters of surface physicals structure of the prepared 50 wt% $LaCoO_3/C_3N_5$ is shown in Table 2. The specific BET

Table 1 $LaCoO_3$ and C_3N_5 conduction band valence band positions

Sample	χ (eV)	E_{CB} (eV)	E_{VB} (eV)	E_g
$LaCoO_3$	5.64	-0.26	2.54	2.80
C_3N_5	4.59	-1.11	1.29	2.40

Table 2 Parameters of surface physicals structure of $LaCoO_3$, C_3N_5 and 50 wt% $LaCoO_3/C_3N_5$

Catalyst	BET surface area (m^2 g^{-1})	Total pore volume (cm^3 g^{-1})	Diameters of pore (nm)
$LaCoO_3$	62.5	0.08	2.26
C_3N_5	56.2	0.06	6.60
50 wt% $LaCoO_3/C_3N_5$	194.5	0.21	2.40

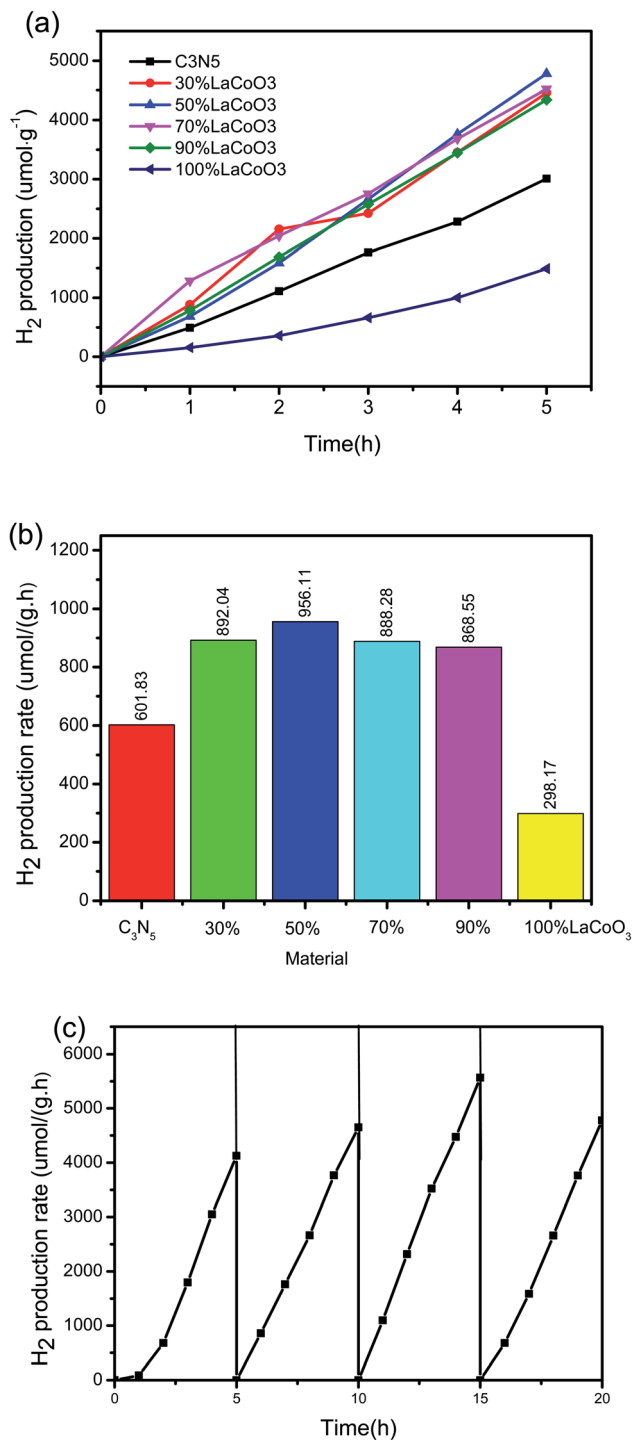© 2022 The Author(s). Published by the Royal Society of Chemistry

Fig. 8 (a) The photocatalytic H_2 release rate of $LaCoO_3$, C_3N_5 and $LaCoO_3/C_3N_5$ composite materials used for water splitting under full-spectrum light irradiation as a function of irradiation time; (b) average hydrogen per hour for different materials productivity; (c) 50% $LaCoO_3/C_3N_5$ long-term stability test for 20 h.

the combination of $LaCoO_3$ and C_3N_5 was beneficial for increasing the active sites, which may improve catalytic activity.

3.8 Evaluation of photocatalytic performance

First, to evaluate the influence of light and catalyst on the experiment, a blank control experiment was carried out without light or a photocatalyst. Photocatalysis plays an important role in improving the efficiency of photocatalysis. Under these experimental conditions, the photolysis efficiency without a photocatalyst is negligible, which indicates that water containing 10% methanol is stable under visible light irradiation. To rule out the possibility of methanol reforming in the full spectrum, an anhydrous control experiment was carried out. We used 30 mL methanol and $LaCoO_3/50\%$ C_3N_5 catalyst for the photocatalysis experiments, and the results showed that no hydrogen is produced. This indicates that the methanol in the experiment is a hole sacrificial agent that consumes holes to promote photocatalytic hydrogen production.
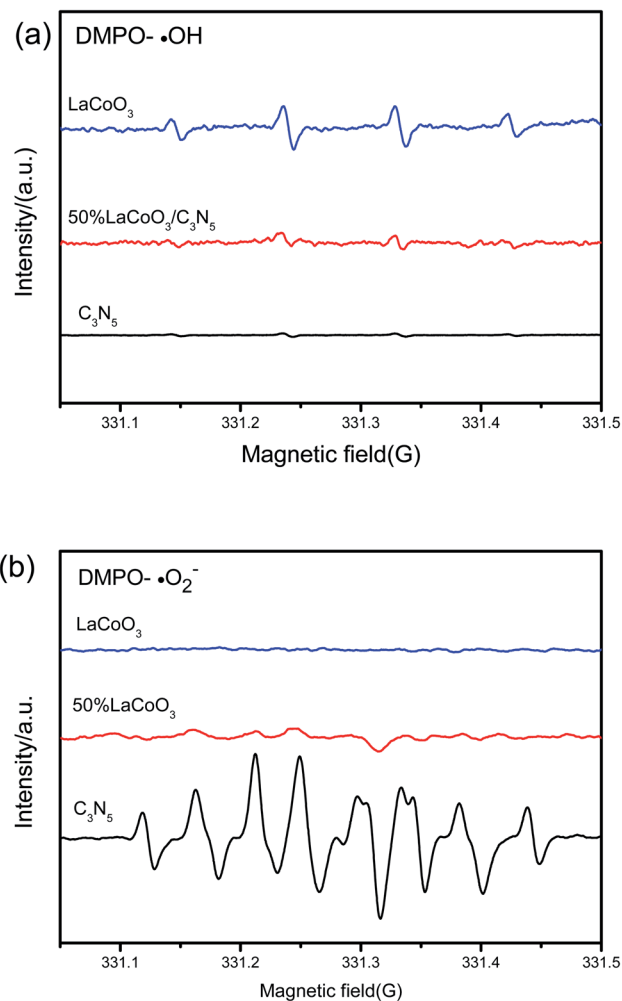

Fig. 9 Use of pure C_3N_5, $LaCoO_3$ and $LaCoO_3/C_3N_5$-50wt% complex in (a) aqueous dispersion (for $BMPO-O^{2-}$) and (b) aqueous dispersion (for $DMPO-\cdot OH$) in xenon lamp full-spectrum illumination.
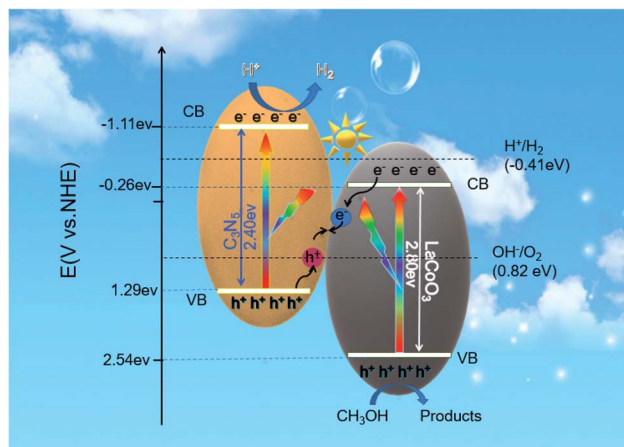
surface area of $LaCoO_3$ and C_3N_5 were 62.5 and 56.2 m^2 g^{-1}, respectively. After the combination, the specific BET surface area of 50 wt% $LaCoO_3/C_3N_5$ was 194.5 m^2 g^{-1}, which was 3.1 times higher than that of $LaCoO_3$. The increase surface area of
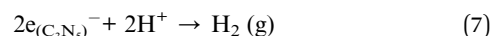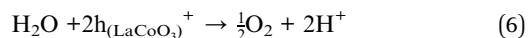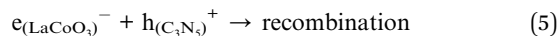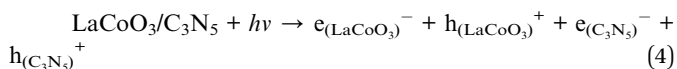
Then, under full-spectrum (250–1200 nm) 300 W xenon lamp irradiation, synthetic $LaCoO_3$, C_3N_5 and $LaCoO_3/C_3N_5$ nanoparticles with different mass ratios were tested in an aqueous solution containing 10% (volume) methanol as a sacrificial reagent. As shown in Fig. 8(a) and (b), a gas chromatograph was used to detect H_2 emissions. We conducted three parallel tests on all samples and calculated the average H_2 escape rate, which can eliminate unexpected factors and obtain more convincing data. Obviously, $LaCoO_3$, C_3N_5 and $LaCoO_3/C_3N_5$ composites prepared with different mass ratios had different levels of hydrogen generation through photolysis. The H_2 release rates of pure $LaCoO_3$ and C_3N_5 were 298.17 µmol h^{-1} g^{-1} and 601.83 µmol h^{-1} g^{-1}, respectively. The $LaCoO_3/C_3N_5$-50wt% composite material has the largest photocatalytic activity, and the average hydrogen production per hour is 956.11 µmol h^{-1} g^{-1}, which is 3.21 and 1.59 times that of $LaCoO_3$ and C_3N_5, respectively. As shown in Fig. 8(c), even after four consecutive cycles, the photocatalytic efficiency did not show a significant loss, which shows that under the full-spectrum irradiation of xenon lamps, the heterojunction photocatalyst is engaged in the photocatalytic hydrolysis process and it is highly stable.

3.9 Electron spin resonance spectrum (ESR) analysis

To understand the mechanism more deeply, electron spin resonance (ESR) spectroscopy was applied. As shown in Fig. 9(a), after 10 minutes of exposure to the full-spectrum light of the xenon lamp, $LaCoO_3$ and $LaCoO_3/C_3N_5$-50wt% DMPO radical ˙OH signals can be observed, but there is no obvious sign of the pure C_3N_5 ˙OH signal. There is no DMPO-˙OH signal in C_3N_5 because ˙OH cannot be generated by holes in C_3N_5's VB ($E_{VB} = 1.67$ eV, $E^{\theta}_{OH^-/OH} = 1.99$ eV $vs.$ NHE). The observation of the DMPO-˙OH signal of the $LaCoO_3/C_3N_5$-50wt% composite shows that the photogenerated holes stay in the VB of $LaCoO_3$ and are not transferred to the VB of C_3N_5. In Fig 9(b), after exposure to the full-spectrum light of the xenon lamp for 10 minutes, the BMPO-O^{2-} signal was observed for the composite sample of C_3N_5 and $LaCoO_3/C_3N_5$-50wt% in the aqueous suspension. The O^{2-} signal of $LaCoO_3$ was observed. The results show that the photogenerated electrons in the composite samples of C_3N_5 and $LaCoO_3/C_3N_5$-50wt% have sufficient reducing power to reduce O_2 to form superoxide radical anions (O^{2-}) ($E^{\theta}_{O_2/O^{2-}} = -0.33$ eV $vs.$ NHE).

The EPR results show that photogenerated electrons and holes exist in C_3N_5 CB and $LaCoO_3$ VB, respectively, and the charge transfer does not follow the conventional type II heterojunction mechanism. Therefore, it can be reasonably considered that the charge transfer path is the Z scheme mechanism. As semiconductors, $LaCoO_3$ and C_3N_5 both have a band-gap. When the photon energy is equal to or greater than the forbidden bandwidth, the photogenerated electrons transition from the VB of C_3N_5 and $LaCoO_3$ to CB and generate holes in the valence band (eqn (4)). Then, the electrons on $LaCoO_3$ quickly recombine with the holes on C_3N_5 through the heterostructure (eqn (5)). The water and holes combine to produce hydrogen ions and oxygen (eqn (6)), and the hydrogen ions further combine with electrons on the conduction band of g-C_3N_4 to

produce hydrogen (eqn (7)). The specific process of photocatalysis is as follows:

$$LaCoO_3/C_3N_5 + hv \rightarrow e_{(LaCoO_3)}^- + h_{(LaCoO_3)}^+ + e_{(C_3N_5)}^- + h_{(C_3N_5)}^+ \quad (4)$$

$$e_{(LaCoO_3)}^- + h_{(C_3N_5)}^+ \rightarrow recombination \quad (5)$$

$$H_2O + 2h_{(LaCoO_3)}^+ \rightarrow \tfrac{1}{2}O_2 + 2H^+ \quad (6)$$

$$2e_{(C_3N_5)}^- + 2H^+ \rightarrow H_2 \text{ (g)} \quad (7)$$

4. Conclusion

In this paper, a new C_3N_5 material was synthesized using the construction of a heterojunction. Starting from the improvement of the semiconductor properties of $LaCoO_3$ and C_3N_5, a composite photocatalyst was successfully prepared, and the photocatalytic activity was significantly improved. X-ray diffraction (XRD) and Fourier transform infrared spectroscopy (FT-IR), scanning electron microscope (SEM), transmission electron microscope (TEM), energy dispersive spectroscopy (EDS), X-ray photoelectron spectroscopy (XPS), ultraviolet visible diffuse reflectance spectroscopy (UV-Vis DRS), transient photocurrent response test, electron spin resonance spectrum (ESR) were applied for a series of characterizations. The characterization results showed that the $LaCoO_3$ prepared by us exists as 50–100 nm nanospheres, and C_3N_5 has a layered structure. The apparent shape of the two was good, confirming the interaction between the heterostructure and the interface of the $LaCoO_3$ nanoparticles and C_3N_5 nanosheets. In the photocatalytic water split test, 50 wt% $LaCoO_3/C_3N_5$ showed the highest photocatalytic activity of 956.11 µmol h^{-1} g^{-1}, which was 3.21 and 1.59 times that of $LaCoO_3$ and C_3N_5, respectively. Even after four consecutive cycles, the photocatalytic efficiency did not show a significant loss, which indicates that the heterojunction photocatalyst is highly stable during the photocatalytic hydrolysis process under the full-spectrum irradiation of xenon lamps. For the $LaCoO_3/C_3N_5$ photocatalytic water splitting system, a Z-type catalytic mechanism was proposed to

explain the significant increase in photocatalytic activity. The novel and effective LaCoO$_3$/C$_3$N$_5$ photocatalyst used in this work can be used in systems for water splitting or other photocatalytic applications. This work not only designs an inexpensive and efficient LaCoO$_3$/C$_3$N$_5$ photocatalytic system for water splitting or other photocatalytic applications, but also provides ideas for constructing new material photocatalytic systems.

Data availability

All data generated or analysed during this study are included in this published article.

Author contributions

RW was the main author of the work, performed syntheses, electron microscopy and coordinated all characterization and catalytic studies. KZ is responsible for part of the synthesis work, XZ and FJ assisted with manuscript writing. All authors read and approved the final manuscript.

Conflicts of interest

The authors listed in the manuscript have declared that they have no competing interests.

References

1 H. Li, *et al.*, Band structure engineering of polymeric carbon nitride with oxygen/carbon codoping for efficient charge separation and photocatalytic performance, *J. Colloid Interface Sci.*, 2020, **564**, 333–343.

2 X. Meng, *et al.*, Carbon quantum dots assisted strategy to synthesize Co@NC for boosting photocatalytic hydrogen evolution performance of CdS, *Chem. Eng. J.*, 2020, **389**, 124432.

3 J. Si, *et al.*, Colour centre controlled formation of stable subnanometer transition metal clusters on TiO$_2$ nanosheet for high efficient H-2 production, *Appl. Surf. Sci.*, 2020, **511**, 145577.

4 M. Chen, *et al.*, A novel Z-scheme AgBr/P-g-C$_3$N$_4$ heterojunction photocatalyst: Excellent photocatalytic performance and photocatalytic mechanism for ephedrine degradation, *Appl. Catal., B*, 2020, **266**, 118614.

5 Z. Cai, *et al.*, Acetate production from inorganic carbon (HCO$_3^-$) in photo-assisted biocathode microbial electrosynthesis systems using WO$_3$/MoO$_3$/g-C$_3$N$_4$ heterojunctions and Serratia marcescens species, *Appl. Catal., B*, 2020, **267**, 118611.

6 Z. Gao, *et al.*, Aminated flower-like ZnIn$_2$S$_4$ coupled with benzoic acid modified g-C$_3$N$_4$ nanosheets *via* covalent

bonds for ameliorated photocatalytic hydrogen generation, *Appl. Catal., B*, 2020, **268**, 118462.

7 A. S. Reddy and J. Kim, An efficient g-C$_3$N$_4$-decorated CdS-nanoparticle-doped Fe$_3$O$_4$ hybrid catalyst for an enhanced H-2 evolution through photoelectrochemical water splitting, *Appl. Surf. Sci.*, 2020, **513**, 145836.

8 M. Tahir, *et al.*, Au-NPs embedded Z-scheme WO$_3$/TiO$_2$ nanocomposite for plasmon-assisted photocatalytic glycerol-water reforming towards enhanced H-2 evolution, *Appl. Surf. Sci.*, 2020, **503**, 144344.

9 H. Li, *et al.*, Band structure engineering of polymeric carbon nitride with oxygen/carbon codoping for efficient charge separation and photocatalytic performance, *J. Colloid Interface Sci.*, 2020, **564**, 333–343.

10 M. Han, *et al.*, Carbon Dots-Implanted Graphitic Carbon Nitride Nanosheets for Photocatalysis: Simultaneously Manipulating Carrier Transport in Inter- and Intralayers, *Sol. RRL*, 2020, 1900517.

11 W. Li, *et al.*, Construction of Z-scheme and p–n heterostructure: Three-dimensional porous g-C$_3$N$_4$/graphene oxide-Ag/AgBr composite for high-efficient hydrogen evolution, *Appl. Catal., B*, 2020, **268**, 118384.

12 P. Kumar, *et al.*, C$_3$N$_5$: A Low Bandgap Semiconductor Containing an Azo-Linked Carbon Nitride Framework for Photocatalytic, Photovoltaic and Adsorbent Applications, *J. Am. Chem. Soc.*, 2019, **141**(13), 5415–5436.

13 S. Qi, *et al*, Metal-free highly efficient photocatalysts for overall water splitting: C$_3$N$_5$ multilayers, *Nanoscale*, 2020, **12**, 306–315.

14 D. Sun, *et al.*, Metal-free boron doped g-C$_3$N$_5$ catalyst: Efficient doping regulatory strategy for photocatalytic water splitting, *Appl. Surf. Sci.*, 2022, **601**(11), 154186.

15 Y. Zhou, *et al.*, A Multiple Structure-Design Strategy towards Ultrathin Niobate Perovskite Nanosheets with Thickness-Dependent Photocatalytic Hydrogen-Evolution Performance, *Chem.–Asian J.*, 2017, **12**(20), 2727–2733.

16 P. Kanhere and Z. Chen, A Review on Visible Light Active Perovskite-Based Photocatalysts, *Molecules*, 2014, **19**(12), 19995–20022.

17 B. Dong, *et al.*, Development of Novel Perovskite-Like Oxide Photocatalyst LiCuTa$_3$O$_9$ with Dual Functions of Water Reduction and Oxidation under Visible Light Irradiation, *Adv. Energy Mater.*, 2018, **8**, 180166035.

18 J. Wang, *et al.*, Double-hole-mediated coupling of anionic dopants in perovskite NaNbO$_3$ for efficient solar water splitting, *Int. J. Quantum Chem.*, 2019, **119**, e2593014.

19 I. M. Nassar, *et al.*, Facile Preparation of n-Type LaFeO$_3$ Perovskite Film for Efficient Photoelectrochemical Water Splitting, *ChemistrySelect*, 2018, **3**(3), 968–972.

20 M. Wang, *et al.*, Hybrid density functional theory description of non-metal doping in perovskite BaTiO$_3$ for visible-light photocatalysis, *J. Solid State Chem.*, 2019, **280**, 121018.

21 N. C. Hildebrandt, J. Soldat and R. Marschall, Layered Perovskite Nanofibers *via* Electrospinning for Overall Water Splitting, *Small*, 2015, **11**(17), 2051–2057.

22 Y. Hu, *et al.*, Layered perovskite oxides and their derivative nanosheets adopting different modification strategies

towards better photocatalytic performance of water splitting, *Renewable Sustainable Energy Rev.*, 2020, **119**, 109527.

23 Y. Cen, *et al.*, Optimized band gap and fast interlayer charge transfer in two-dimensional perovskite oxynitride Ba_2NbO_3N and Sr_2NbO_3/Ba_2NbO_3N bonded heterostructure visible-light photocatalysts for overall water splitting, *J. Colloid Interface Sci.*, 2019, **546**, 20–31.

24 J. Xu, *et al.*, Perovskite Oxide $LaNiO_3$ Nanoparticles for Boosting H-2 Evolution over Commercial CdS with Visible Light, *Chem.–Eur. J.*, 2018, **24**(69SI), 18512–18517.

25 K. Maeda, M. Eguchi and T. Oshima, Perovskite Oxide Nanosheets with Tunable Band-Edge Potentials and High Photocatalytic Hydrogen-Evolution Activity, *Angew. Chem., Int. Ed.*, 2014, **53**(48), 13164–13168.

26 S. N. Tijare, *et al.*, Photocatalytic hydrogen generation through water splitting on nano-crystalline $LaFeO_3$ perovskite, *Int. J. Hydrogen Energy*, 2012, **37**(13), 10451–10456.

27 J. Guo, *et al.*, Synthesis and characterization of Ag_3PO_4/$LaCoO_3$ nanocomposite with superior mineralization potential for bisphenol A degradation under visible light, *J. Alloys Compd.*, 2017, **696**, 226–233.

28 R. Wang, *et al.*, Z-Scheme $LaCoO_3$/g-C_3N_4 for Efficient Full-Spectrum Light-Simulated Solar Photocatalytic Hydrogen Generation, *ACS Omega*, 2020, **5**(47), 30373–30382.

29 R. R. Solís, *et al.*, Synergism between peroxymonosulfate and $LaCoO_3$-TiO_2 photocatalysis for oxidation of herbicides. Operational variables and catalyst characterization assessment, *J. Chem. Technol. Biotechnol.*, 2017, **92**(8), 2159–2170.

30 B. Dong, *et al.*, Highly Efficient $LaCoO_3$ Nanofibers Catalysts for Photocatalytic Degradation of Rhodamine B, *J. Am. Ceram. Soc.*, 2010, **93**(11), 3587–3590.

31 J. Guo, P. Li and Z. Yang, A novel Z-scheme g-C_3N_4/$LaCoO_3$ heterojunction with enhanced photocatalytic activity in degradation of tetracycline hydrochloride, *Catal. Commun.*, 2019, **122**, 63–67.

32 H. Lan, *et al.*, Microstructure of carbon nitride affecting synergetic photocatalytic activity: Hydrogen bonds *vs.* structural defects, *Appl. Catal., B*, 2017, **204**, 49–57.

33 L. Wang, *et al.*, Experimental study on the high performance of Zr doped $LaCoO_3$ for solar thermochemical CO production, *Chem. Eng. J.*, 2020, **389**, 124426.

34 J. Luo, *et al.*, Utilization of $LaCoO_3$ as an efficient co-catalyst to boost the visible light photocatalytic performance of g-C_3N_4, *Sep. Purif. Technol.*, 2018, **201**, 309–317.

35 C. Belver, *et al.*, Innovative W-doped titanium dioxide anchored on clay for photocatalytic removal of atrazine, *Catal. Today*, 2017, **280**, 21–28.

36 Y. Hong, *et al.*, *In situ* synthesis of direct solid-state Z-scheme V_2O_5/g-C_3N_4 heterojunctions with enhanced visible light efficiency in photocatalytic degradation of pollutants, *Appl. Catal., B*, 2016, **180**, 663–673.

37 J. Zhu, *et al.*, Enhancing CO_2 catalytic activation and direct electroreduction on *in situ* exsolved Fe/MnO_x nanoparticles from $(Pr,Ba)_2Mn_{2-y}Fe_yO_{5+\delta}$ layered perovskites for SOEC cathodes, *Appl. Catal., B*, 2020, **268**, 118389.